Cytoarchitectonic Maps of the Human Metathalamus in 3D Space

Kai Kiwitz[1,2]*, Andrea Brandstetter[3], Christian Schiffer[3,4], Sebastian Bludau[3], Hartmut Mohlberg[3], Mona Omidyeganeh[5,6], Philippe Massicotte[5] and Katrin Amunts[1,2,3]

[1] Cécile and Oskar Vogt Institute of Brain Research, University Hospital Düsseldorf, Medical Faculty, Heinrich Heine University, Düsseldorf, Germany, [2] Max Planck School of Cognition, Stephanstraße 1a, Leipzig, Germany, [3] Institute of Neuroscience and Medicine (INM-1), Forschungszentrum Jülich, Jülich, Germany, [4] Helmholtz AI, Forschungszentrum Jülich, Jülich, Germany, [5] McGill Centre for Integrative Neuroscience, McConnell Brain Imaging Center, Montreal Neurological Institute, McGill University, Montreal, QC, Canada, [6] National Research Council of Canada, Ottawa, ON, Canada

The human metathalamus plays an important role in processing visual and auditory information. Understanding its layers and subdivisions is important to gain insights in its function as a subcortical relay station and involvement in various pathologies. Yet, detailed histological references of the microanatomy in 3D space are still missing. We therefore aim at providing cytoarchitectonic maps of the medial geniculate body (MGB) and its subdivisions in the BigBrain – a high-resolution 3D-reconstructed histological model of the human brain, as well as probabilistic cytoarchitectonic maps of the MGB and lateral geniculate body (LGB). Therefore, histological sections of ten postmortem brains were studied. Three MGB subdivisions (MGBv, MGBd, MGBm) were identified on every 5th BigBrain section, and a deep-learning based tool was applied to map them on every remaining section. The maps were 3D-reconstructed to show the shape and extent of the MGB and its subdivisions with cellular precision. The LGB and MGB were additionally identified in nine other postmortem brains. Probabilistic cytoarchitectonic maps in the MNI "Colin27" and MNI ICBM152 reference spaces were computed which reveal an overall low interindividual variability in topography and extent. The probabilistic maps were included into the Julich-Brain atlas, and are freely available. They can be linked to other 3D data of human brain organization and serve as an anatomical reference for diagnostic, prognostic and therapeutic neuroimaging studies of healthy brains and patients. Furthermore, the high-resolution MGB BigBrain maps provide a basis for data integration, brain modeling and simulation to bridge the larger scale involvement of thalamocortical and local subcortical circuits.

Keywords: metathalamus, BigBrain, cytoarchitectonic maps, lateral geniculate body, medial geniculate body, human, 3D histology

INTRODUCTION

The human metathalamus, located caudoventrally of the main body of the thalamus, plays an important role in processing visual and auditory information. Visual and auditory processing is encoded separately in the two major nuclei of the metathalamus, i.e., the lateral geniculate body (LGB) and the medial geniculate body (MGB). The LGB is a 6-layered structure, innervated by optic tract fibers covering the contralateral visual field. Its two magnocellular and four parvocellular layers process functionally distinct retinal pathways. The MGB on the other hand receives input from ascending tonotopically organized projections *via* the medial lemniscus, as well as projections

from the inferior colliculus and the auditory cortex (Peruzzi et al., 1997; Saint Marie et al., 1997; Llano and Sherman, 2008; Caspary and Llano, 2017). It can cytoarchitectonically be subdivided into three major compartments: the ventral, dorsal and medial subdivisions (Winer, 1984). Both nuclei have prominent projections to cortical areas and serve as subcortical relay stations.

Investigating the structural-functional relationship of the MGB and LGB including its subdivisions and layers is also relevant from a clinical perspective, e.g., to understand the MGB's involvement in tinnitus (Llinas et al., 2002; Rauschecker et al., 2010; Leaver et al., 2011; Ridder et al., 2015; Caspary and Llano, 2017; Berlot et al., 2020), speech recognition (Mihai et al., 2019), and developmental dyslexia (Díaz et al., 2012) as well as the LGB's role in glaucoma (Wang et al., 2015; Stein et al., 2021), multiple sclerosis (Korsholm et al., 2007; Papadopoulou et al., 2019), Parkinson's (Lee et al., 2016), and psychiatric diseases (Butler and Javitt, 2005; Selemon and Begovic, 2007).

Since the spatial resolution of ultra-highfield fMRI has increased to the submillimeter range in recent years, more detailed studies have been become feasible including the possibility to measure laminar brain activity (Huber et al., 2018; Jia et al., 2021) as well as identifying functional subdivisions of subcortical (Rijk et al., 2021) and cortical (Martino et al., 2015; Nasr et al., 2016) structures.

However, existing histological maps of the human thalamus do not include subdivisions of the MGB and/or layers of the LGB or do not cover the metathalamus over its whole extent (Morel, 2007; Krauth et al., 2010; Ding et al., 2016; Mai et al., 2016). The same holds true for MRI based probabilistic atlases of the thalamus (Iglesias et al., 2018; Najdenovska et al., 2018; García-Gomar et al., 2019). Furthermore, no probabilistic histologically based reference maps of the metathalamus exist so far, which make it difficult to account for individual variability in topography and volume, as well as to compare histological maps with findings from neuroimaging. More detailed maps of subdivisions and layers of the MGB and LGB could provide micro-anatomical reference data for high-field MRI investigations, to inform neuroimaging studies, and to provide reference data for biologically realistic brain modeling and simulation.

The BigBrain model based on its 7404 cell-body stained and 3D-reconstructed sections constitutes an anatomical brain model at a spatial resolution of 20 micrometers isotropic in this regard (Amunts et al., 2013). It has been used, for example, to interpret MRI based models of brain connectivity (Wei et al., 2019; Paquola et al., 2020b), functional and structural gradients (Paquola et al., 2019; Royer et al., 2020), as well as default mode network components (Margulies et al., 2016; Paquola et al., 2019).

In the present study, we aimed to create a cytoarchitectonic map of the MGB and its subdivisions in the BigBrain model and supplement previously published maps of the LGB with its six layers (Brandstetter et al., 2021). To construct a high-resolution map of the MGB, a novel deep-learning based cytoarchitectonic mapping tool was applied (Schiffer et al., 2021c). Secondly, the MGB and LGB were identified in histological sections of ten postmortem brains and volumes, as

well as probabilistic cytoarchitectonic maps were computed to address the intersubject variability of the two nuclei.

MATERIALS AND METHODS

Processing of Postmortem Brains

Cytoarchitectonic mapping was performed in serial histological sections of ten human brains from body donors (5 female, age 59–85 years, 5 male, 30–75 years, **Table 1**). The brains were obtained in accordance to legal and ethical regulations and guidelines as part of the body donor program of the Department of Anatomy of the Heinrich Heine University Düsseldorf. Body donors gave written informed consent for the general use of brain tissue for aims of research and education. All usage in this work is covered by a vote of the ethics committee of the Medical Faculty of the Heinrich Heine University Düsseldorf (#4863). The postmortem delay did not exceed 24–36 h. The list of brains also included the BigBrain dataset (Amunts et al., 2013).

The procedure of processing the brain tissue was described in detail in Amunts et al. (2020). In short, the brains were fixed in 4% buffered formalin (pH 7.4) or Bodian's fixative for at least 3 months. All brains underwent magnetic resonance imaging using a T1-weighted 3D FLASH sequence (flip angle 40°, repetition time TR 40 ms, echo time TE 5 ms). MR images were used as an undistorted spatial reference for the 3D-reconstruction of the histological sections. After scanning, the brains were embedded in paraffin and serially sectioned in the coronal plane on a large-scale microtome (20 μm thickness), whereby series of blockface images of the paraffin-embedded brains were obtained. Every 15th section (every section in case of the BigBrain) was stained for cell bodies using a silver staining technique (Merker, 1983), and digitized using tissue scanners (1 μm in-plane resolution).

Cytoarchitectonic Probability Maps

To create probability maps of the MGB and LGB, both nuclei were delineated and traced over their whole extent on every 15th section (distance between sections: 300 μm) in all 10

TABLE 1 | List of postmortem brains used for cytoarchitectonic mapping and analysis.

Brain ID	Gender	Age (Years)	Cause of death	Fresh weight (g)
pm 1	Female	79	Carcinoma of the bladder	1,350
pm 4	Male	75	Necrotizing glomerulonephritis	1,349
pm 5	Female	59	Cardiorespiratory insufficiency	1,142
pm 7	Male	37	Acute right heart failure/cardiac arrest	1,437
pm 8	Female	72	Renal failure/renal arrest	1,216
pm 9	Female	79	Cardiorespiratory insufficiency	1,110
pm 10	Female	85	Mesenteric infarction	1,046
pm 13	Male	39	Drowning	1,234
pm 20	Male	65	Cardiorespiratory insufficiency	1,392
pm 21	Male	30	Bronchopneumonia	1,409

brains using an in-house software (Online Section Tracer). The MGB was identified based on previous microscopical studies and its characteristic topography (Kuhlenbeck, 1954; Winer, 1984). Delineation criteria for the LGB were adapted from the literature (Clark, 1932; Brandstetter et al., 2021). The delineations of the MGB and LGB in the left and the right hemisphere were 3D-reconstructed. Hereby, spatial transformations of the whole-brain histological datasets were used that were earlier computed based on the MR-images and the blockface images of the paraffin-embedded brains. The delineated nuclei were then spatially normalized and transferred to the T1-weighted single-subject template of the Montreal Neurological Institute (MNI), "Colin27", as well as the MNI ICBM152 2009c non-linear asymmetric reference space (Evans et al., 2012). The individual maps of the MGB and the LGB were superimposed in both templates to calculate probabilistic maps. Values from 0 to 100% overlap were calculated to indicate the probability for each voxel of the reference brain to contain either the MGB or the LGB at a certain position (Amunts et al., 2020).

Volumetric Analysis

Volumes were calculated and corrected for shrinkage based on the delineations of the MGB and LGB in histological sections based on Cavalieri's principle (Amunts et al., 2007). A volume normalization was applied by calculating the proportion of the volume of the structures and the total brain volume to make the results comparable (Bludau et al., 2014). Differences in volume proportions were tested for significant effects caused by hemisphere (left vs. right) and sex (male vs. female) with pair-wise permutation tests. For each of these tests, the corresponding values (male/female; left/right hemisphere) were grouped and a contrast estimate was calculated between the means of these groups. The null distribution was estimated by a Monte-Carlo simulation. All values were randomly redistributed into two groups, calculating the same contrast with a repetition of 1,000,000 iterations. Differences were considered statistically significant if the contrast estimate of the true comparison was larger than 95% of the values under the null distribution ($p < 0.05$). Differences in mean volumes between the MGB and LGB were analyzed using a paired two-sided t-test with an α error-rate set to 0.05.

High-Resolution Cytoarchitectonic Brain Mapping in the BigBrain

In addition, the MGB and its subdivisions were delineated on every 5th section of the BigBrain dataset (Amunts et al., 2013) using the high-resolution digitized scans. The range of sections covered a distance of 3.20 mm in the left and 3.08 mm in the right hemisphere. To map the three subdivisions on every section, a deep-learning based brain mapping tool designed to map cytoarchitectonic structures in full stacks (Schiffer et al., 2021c) was applied. The deep-learning network architecture has shown to resemble cytoarchitectonic criteria (Kiwitz et al., 2020) and has successfully been used to generate whole-stack maps of several cytoarchitectonic areas (Schiffer et al., 2021c). The method was trained on 57 delineated sections containing the

MGB and its subdivisions. Training was performed remotely *via* a web-based interface (Schiffer et al., 2021c) on the supercomputer JURECA at Jülich Supercomputing Centre (Krause and Thörnig, 2018). Automatically created maps were subsequently controlled to exclude falsely qualified sections, which were manually corrected *via* the tool's web-based interface. The annotations were transformed into the 3D-reconstructed BigBrain space by applying a non-linear registration of the high-resolution digitized sections (Omidyeganeh et al., 2020) and available transformations for the BigBrain (Amunts et al., 2013) to generate a volume for each MGB subdivision. The total number of volume voxels, their physical size and a shrinkage factor of 1.931 for the BigBrain (Bludau et al., 2014) were subsequently used to calculate the volume of the MGB and its subdivisions. The total volume of the subdivisions of this straight-forward approach was compared to the estimated MGB volume based on Cavalieri's principle as described above.

3D-surface meshes of the subdivisions were generated using the marching cube algorithm (Lewiner et al., 2003). The 3D reconstruction directly followed the protocol described in Schiffer et al. (2021c). Rough edges on the mesh surfaces were subsequently smoothed locally using normalized curvature operators in the normal direction preserving their specific structure. Surface meshes of the LGB have been generated and 3D-reconstructed in a similar manner based on publicly available whole brain maps of the LGB and its layers in the BigBrain (Brandstetter et al., 2021; Schiffer et al., 2021a).

RESULTS

Localization of the Medial and Lateral Geniculate Bodies

The MGB and LGB followed a consistent topography in all analyzed postmortem brains. The LGB was located ventrolaterally of the pulvinar of the thalamus. It showed the typical 6-layered pattern with sharp bends. The MGB was always located medially to the LGB. Its caudal pole protruded from the caudal extremity of the diencephalon. The caudal pole itself was located caudoventrally of the posterior nuclear complex (i.e., the compact limitans, suprageniculate and posterior nucleus of the thalamus) and medially of the inferior pulvinar nucleus of the thalamus (**Figure 1**). The caudal surface of the pretectum formed the dorsomedial flank of the MGB.

Probabilistic Cytoarchitectonic Maps of the Medial and Lateral Geniculate Bodies

Delineations of the MGB and LGB in the sample of 10 postmortem brains were transferred to the MNI Colin 27 and MNI ICBM152 2009c non-linear asymmetric reference spaces. The probability maps of the two nuclei show their paired arrangement caudoventrally of the main body of the thalamus. The LGB is located dorsally of the hippocampal formation along its whole extent with the MGB adjoining it medially (**Figure 2**). Center of mass coordinates in the Colin 27 and MNI ICBM152 2009c non-linear asymmetric spaces (in parentheses) constituted
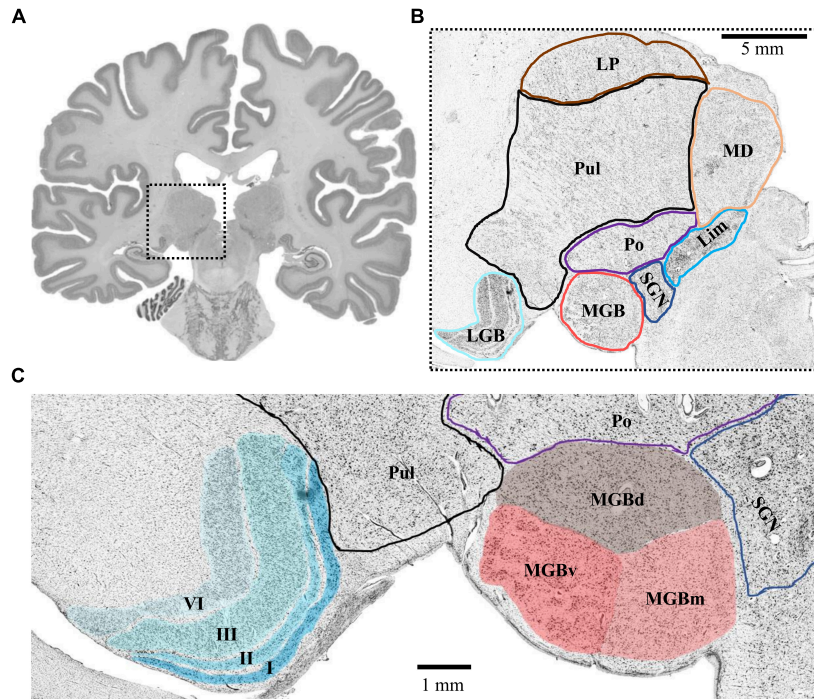
FIGURE 1 | Topography of the MGB and LGB. **(A)** Cell-body stained section (number 3660, caudal MGB) from the left hemisphere of postmortem brain pm 21. The dashed box indicates the location of the thalamus magnified in panel **(B)**. **(B)** Magnified crop from panel **(A)** showing the topography of the MGB and LGB (cyan and red) in comparison to putative locations of other thalamic nuclei. **(C)** Magnified crop from panel **(B)** depicting the layered structure of the LGB (cyan, left side) and the subdivisions of the MGB (red, right side). Roman numerals indicate layers of the LGB; LGB, lateral geniculate body; MGB, medial geniculate body; MGBv, ventral subdivision of the MGB; MGBd, dorsal subdivision; MGBm, medial subdivision; Po, posterior nucleus; SGN, suprageniculate nucleus; Lim, compact limitans nucleus; Pul, pulvinar; MD, mediodorsal nucleus; LP, lateral posterior nucleus.
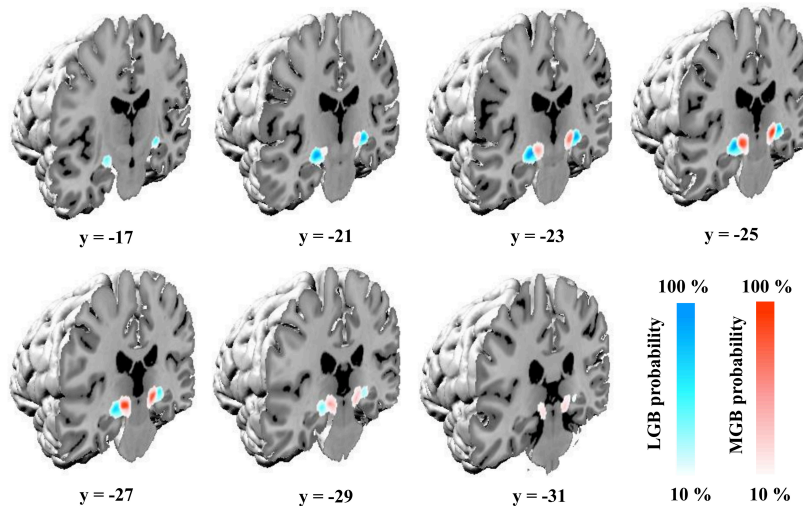

FIGURE 2 | Probability maps of the MGB and LGB in the single-subject template of MNI "Colin27" (Evans et al., 2012). Coronal slices from rostral ($y = -17$) to caudal ($y = -31$) show the probability maps color-coded in blue (LGB) and red (MGB) in the MNI "Colin27" coordinate space. Color gradients on the lower right indicate the overlap across the ten postmortem brains for a specific voxel (10%: only one brain; 100%: all ten brains); LGB, lateral geniculate body; MGB, medial geniculate body.

$x = -24$, $y = -24$, $z = -10$ (-24, -25, -9) for he left LGB, $x = 22$, $y = -24$, $z = -10$ (23, -24, -9) for the right LGB, $x = -16$, $y = -27$, $z = -8$ (-15, -27, -7) for the left MGB, as well as $x = 14$, $y = -27$, $z = -9$ (15, -26, -8) for the right MGB. The y-coordinates of the center of masses demonstrate the more rostral location of the LGB ($y = -24$) in comparison to the MGB

TABLE 2 | Mean volumes, standard deviations (SD) as well as minimal and maximal values of the shrinkage-corrected mean volumes of the MGB and LGB in ten postmortem brains for both hemispheres measured in mm^3.

Nucleus	Statistic	Left hemisphere	Right hemisphere	Sum
MGB	Mean	124.3	134.4	258.7
	Min	91.9	89.0	
	Max	164.2	209.3	
	SD	27.4	35.3	59.2
LGB	Mean	166.9	165.5	332.4
	Min	116.3	120.4	
	Max	220.8	218.3	
	SD	28.5	26.6	54.6

MGB, medial geniculate body; LGB, lateral geniculate body.

($y = -27$) as shown in **Figure 2**. The color-coded probability maps of both nuclei (**Figure 2**) show a central peak with a steady decrease when moving away from the center of mass in all three dimensions – emphasizing the central location of the two nuclei within the probability maps in both hemispheres.

Volumetric Analysis of the Metathalamus

Results of the volumetric analysis of the ten postmortem brains are shown in **Table 2**. Shrinkage-corrected mean volumes of the MGB (Mean = 258.7 mm^3, SD = 59.2 mm^3) were significantly smaller than the LGB (Mean = 332.4 mm^3, SD = 54.6 mm^3) volumes ($t(9) = -7.0$, $p < 0.001$, two-sided test). Permutation tests did not reveal any significant effects of hemisphere and sex as well as their interaction on the shrinkage-corrected volumes for each nucleus ($p > 0.05$).

Cytoarchitecture of the Medial Geniculate Body

Three subdivisions of the MGB were identified and delineated in the BigBrain (**Figure 3**): The ventral subdivision (MGBv) formed the ventrolateral part of the MGB and was mainly comprised of small and medium sized perikarya, some of which formed row-like clusters as described previously (Winer, 1984). These contributed to a layer-like appearance of the ventral subdivision (**Figure 3B**). The MGBv was flanked by white matter that extended ventrally to the lateral border of the cerebral peduncle and ringed the free surface of the caudal pole of the MGB (**Figure 3G**). It could easily be separated from the medial and dorsal subdivisions by cell-sparse zones (**Figure 3H**), as well as differences in cell-density, size and composition. Similar to observations by Winer (1984), we found a small cluster of larger cells in the ventrolateral part of the ventral subdivision on some sections (**Figure 3E**).

The dorsal subdivision (MGBd) covered the whole caudo-rostral extent of the MGB forming a cap on top of the ventral and medial subdivisions. It showed a reduced cell-density in comparison to the ventral subdivision (**Figure 3C**). The largest cells in the dorsal subdivision could be found on the medial and ventromedial limb, right at the border to the medial subdivision (**Figure 3F**). They marked the border to the medial subdivision. The border to the medial subdivision was also characterized

by a fine cell-sparse zone, which was more profound in rostral sections (**Figure 3F**).

The medial subdivision (MGBm) formed the ventromedial part of the MGB and, on average, contained the largest perikarya of all subdivisions (**Figure 3D**). The MGBm showed a caudo-rostral gradient of increasing cell size which facilitated the separation from the ventral subdivision in rostral sections. At the same time, the increase in cell size impeded the separation from the dorsal subdivision with its especially large somata at the border to the medial subdivision (**Figure 3F**).

High-Resolution 3D-Reconstructions of the Medial Geniculate Body in the BigBrain

The deep-learning based brain mapping tool allowed to identify delineations of the three subdivisions of the MGB on 132 sections of the left and 165 sections of the right hemisphere in the BigBrain. Combined 3D-reconstructions of the MGB and LGB (Brandstetter et al., 2021) with its subdivisions and layers in the BigBrain are shown in **Figure 4** (see **Supplementary Video**) and demonstrate the paired arrangement of the two nuclei in proximity of the hippocampal formation ventrolaterally (**Figure 4C**). The MGBd forms a cap across the whole extent of the MGB. The ventral and medial subdivisions share the lower half of the MGB. On rostral sections, MGBd and MGBm are flanked by white matter and parts of the ventrobasal complex of the thalamus (**Figure 4C**). Here, the darkly stained substantia nigra of the mesencephalon can be seen ventromedially of the MGB (**Figure 4C**). Caudally, the MGBd and MGBm border the posterior nuclear complex along their dorsomedial surface, whereas the MGBd and MGBv border the most caudal tip of the inferior pulvinar nucleus (see **Figures 1B,C** for an illustration).

Shrinkage-corrected volumes of MGBv and MGBm were larger in the left hemisphere, whereas the MGBd subdivision showed a similar size in both hemispheres (**Table 3**). The sum of all three subdivisional volume measurements corresponds to the mean MGB volume calculated based on mappings on every 15th section in postmortem brain pm20 (BigBrain). The latter fits within 0.8 standard deviations of the left and 1.3 standard deviations of the right hemisphere of the mean volume measurements based on all ten postmortem brains (**Table 2**).

DISCUSSION

The present study introduces high-resolution 3D brain maps of the human MGB and its subdivisions in the BigBrain utilizing a novel deep-learning based brain mapping tool. Together with the recently published LGB layer maps (Brandstetter et al., 2021) they provide a high-resolution whole-brain histological reference of the metathalamus at 20 micrometer resolution. Additionally, probabilistic cytoarchitectonic maps of the MGB and LGB were calculated in a sample of ten brains, with a spatial resolution of 1 mm. They have been aligned with two commonly used reference spaces (MNI "Colin27" and MNI ICBM152 2009c non-linear asymmetric) and are part the Julich-Brain atlas (Amunts et al., 2020). All datasets are publicly available on
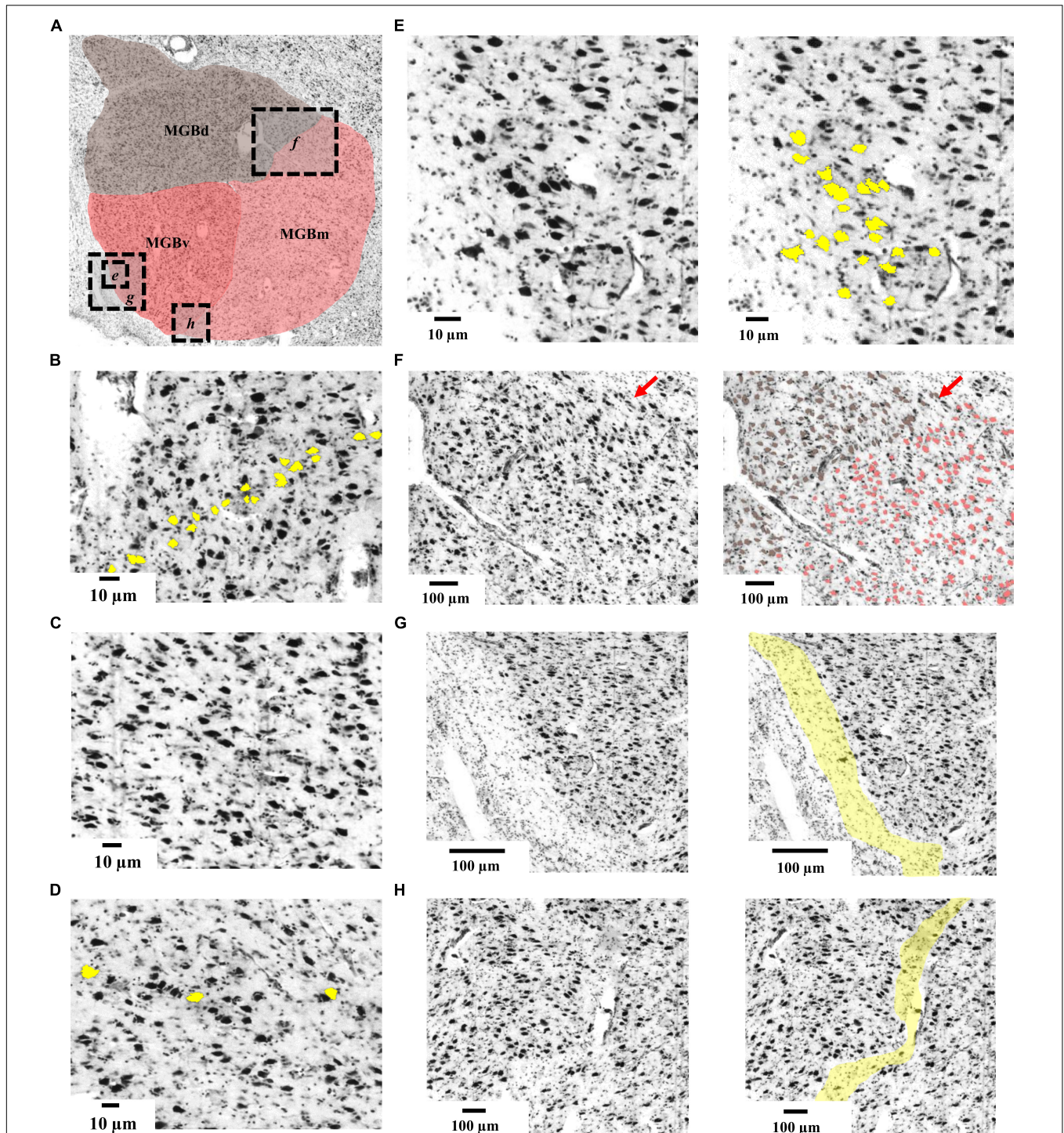
FIGURE 3 | Cytoarchitecture of the MGB. **(A)** Histological cell-body stained section from the left hemisphere of the BigBrain (section 3290, rostral level of the MGB) displaying the three subdivisions. Dashed boxes with italic letters (e-h) indicate magnified excerpts. **(B)** Cytoarchitecture of MGBv showing row-like clusters of medium-sized cells (yellow); **(c)** cytoarchitecture of MGBd showing a cell-sparse pattern. **(D)** Cytoarchitecture of MGBm showing perikarya (yellow) which were larger than in the other subdivisions. **(E)** Magnified excerpts from the ventrolateral quadrant of MGBv showing the putative human homologous region of the feline ventrolateral nucleus (Winer, 1984). **(F)** Magnified excerpts of the border between MGBd and MGBm. Red arrows indicate a cell-sparse zone defining the borderline. Brownish colored cells correspond to the previously described suprageniculate and posterior limitans nuclei of MGBd (Winer, 1984) and are of similar size as the reddish colored cells of MGBm. **(G)** Magnified excerpts from the ventrolateral part of MGBv showing a capsule of neuropil (yellow) flanking MGBv. **(H)** Magnified excerpts of the border between MGBv and MGBm highlighting a cell-sparse zone that defines the borderline; MGB, medial geniculate body; MGBv, ventral subdivision of the MGB; MGBd, dorsal subdivision; MGBm, medial subdivision.
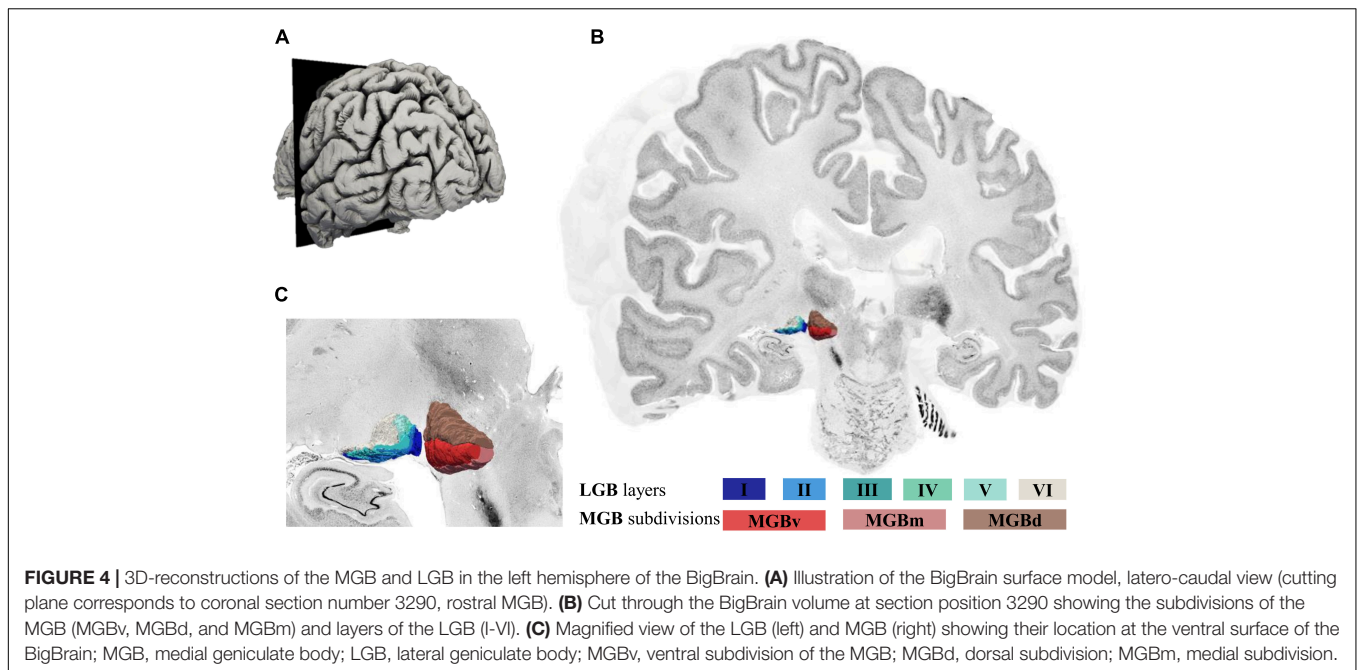
FIGURE 4 | 3D-reconstructions of the MGB and LGB in the left hemisphere of the BigBrain. **(A)** Illustration of the BigBrain surface model, latero-caudal view (cutting plane corresponds to coronal section number 3290, rostral MGB). **(B)** Cut through the BigBrain volume at section position 3290 showing the subdivisions of the MGB (MGBv, MGBd, and MGBm) and layers of the LGB (I-VI). **(C)** Magnified view of the LGB (left) and MGB (right) showing their location at the ventral surface of the BigBrain; MGB, medial geniculate body; LGB, lateral geniculate body; MGBv, ventral subdivision of the MGB; MGBd, dorsal subdivision; MGBm, medial subdivision.

TABLE 3 | Volumes of the MGB subdivisions in the BigBrain for both hemispheres.

MGB subdivision	Volume in mm³	
	Left hemisphere	Right hemisphere
MGBv	18.7	13.1
MGBd	44.8	45.3
MGBm	39.6	31.6
Sum of subdivisions	103.1	90.0

Measurements show shrinkage-corrected volumes obtained from the 3D-reconstructed surface meshes of the MGB subdivisions (MGBv, MGBd, and MGBm); MGB, medial geniculate body; MGBv, ventral subdivision of the MGB; MGBd, dorsal subdivision; MGBm, medial subdivision.

EBRAINS (Kiwitz et al., 2021b; Schiffer et al., 2021b) and the multi-level atlas of the Human Brain Project.[1]

Comparison With Previous Histological Studies and Atlases

The overall characterization of three distinct subdivisions of the MGB in the BigBrain is in accordance to histological studies in human (Hassler, 1959; Winer, 1984; Morel, 2007; Ding et al., 2016; Mai et al., 2016) and animal brains (Morest, 1964; Clerici and Coleman, 1990). The topography of the three MGB subdivisions in the BigBrain resembles that shown by Morel (2007), Hassler (1959), and Winer (1992). Following their localization of the subdivisions, our analysis consolidates the notion for the ventromedial location of the magnocellular subdivision MGBm. This subdivision has previously also been reported to be located more ventrolateral by Amunts et al. (2012). The cytoarchitectonic features in our investigation correspond

well with those found by Winer (1984), with the exception of the described size of perikarya in MGBm. In the BigBrain, MGBm still contains the largest perikarya of all subdivisions, yet the size difference seems to be not as distinct as previously described (Winer, 1984). Although we were able to detect some correspondences to even finer subparcellations, i.e., the suprageniculate and posterior limitans nuclei of the dorsal subdivision (**Figure 3F**) and a cell cluster possibly corresponding to the feline ventrolateral nucleus (Strick and Sterling, 1974; Winer, 1984), further subdivisions found in human (Winer, 1984) and animal studies (Morest, 1964; Harrison and Howe, 1974) could not reliably be replicated in the BigBrain.

Intersubject Variability of Volumes

Currently available histological atlases mostly contain metathalamic structures based on single brains (Ding et al., 2016) with the exception of Morel (2007), who compared the topography of structures to a previously published atlas using a different postmortem brain. The present analysis addresses intersubject variability in a larger sample. The here provided shrinkage-corrected mean volumes of the MGB add to the limited literature of histological volume measurements (Glendenning and Masterton, 1998; Rademacher et al., 2002; Sitek et al., 2019). The interindividual variability in MGB volume resembles data of a more than twofold variability reported earlier (Rademacher et al., 2002). The same is true for the LGB volumes and their approximately twofold interindividual variation (Zvorykin, 1980; Andrews et al., 1997). Similar to previous histological investigations, we found no significant hemispheric asymmetries of MGB and LGB volumes (Eidelberg and Galaburda, 1982; Andrews et al., 1997; Rademacher et al., 2002).

At the same time, volume measurements derived from MRI-based measurements differ to a varying degree from our histological volumes. Comparable MGB volumes have been reported using postmortem MRI (Sitek et al., 2019) and structural *in vivo* MRI (Kitajima et al., 2015; Amaral et al., 2016). At the same time higher MGB, as well as higher and lower LGB volumes have been reported using functional and structural *in vivo* MR measurements (Li et al., 2012; García-Gomar et al., 2019; Jonak et al., 2020).

These inconsistencies may reflect the inherent difficulty of manually segmenting small subcortical nuclei in MR-images. A direct localization of the LGB in structural MR images under low field strengths (1.5 Tesla) requires prior enhancement and co-registration to anatomical surroundings (Li et al., 2012). At 3 Tesla, the LGB has been delineated indirectly using prior masking (Wang et al., 2015; Cecchetti et al., 2016). A more direct segmentation of the LGB and MGB using structural and diffusion-weighted imaging becomes feasible at higher (7 Tesla) field strengths (García-Gomar et al., 2019). Although the MGB becomes detectable at such field strengths, a clear segmentation has only been reported for postmortem structural MR (Sitek et al., 2019). Yet, even under high field strengths a histological validation still seems to be needed to rule out possible confounds such as low diffusion anisotropy due to crossing fibers, as well as to assist investigators with anatomical landmark information when creating segmentations (García-Gomar et al., 2019). The task difficulty of perceiving the LGB and MGB in MR images is significantly impacted by the image acquisition procedure (Kitajima et al., 2015) – imposing a threat to the objectivity of such segmentations. Therefore, *in vivo* segmentations of metathalamic nuclei in particular for the MGB remains challenging due to the nuclei's small size and low contrast - confirming the notion for a more precise histologically derived reference that our probability maps provide.

The new maps constitute a probabilistic representation of the MGB and LGB in the general population and include five female and five male donors with a wide age range including brains from older body donors. The older age of some body donors may raise the question of possible structural changes of the MGB in the context of age-related hearing loss. Several studies indicate age-related changes of the subcortical auditory system with regards to neurotransmitter and calcium-binding protein expression (reviewed in Caspary and Llano, 2019). Both for normal aging and pathological conditions such as deafness, structural changes have been reported for the temporal cortex including the primary auditory cortex (Lin et al., 2014; Wong et al., 2014; Qian et al., 2017), but not for the MGB (Stanton and Harrison, 2000; Butler and Lomber, 2013; Caspary and Llano, 2019). Other pathologies like Alzheimer's disease and Leber's hereditary disease have shown to alter human MGB volumes (Jonak et al., 2020; Bernstein et al., 2021). The clinical records of the body donors did not include any information of such pathologies, and did not mention any changes in hearing abilities. Therefore, the here presented volumes seem to represent mean volumes of the investigated age range.

Neuroscientific and Clinical Relevance

The maps are part of the Julich-Brain (Amunts et al., 2020), an atlas that is part of the multilevel atlas of the Human Brain Project and its research infrastructure EBRAINS.[2] This way, the maps may provide a reference to localize findings from neuroimaging and serve as seed regions for functional connectivity and diffusion weighted imaging analyses. In this regard, they can be used to study brain disorders and functional impairments, including the LGB's involvement in visual field and eye movement deficits (Dai et al., 2011; Pasu et al., 2015; Usrey and Alitto, 2015; Wang et al., 2015), multiple sclerosis (Sepulcre et al., 2009; Hickman et al., 2014; Papadopoulou et al., 2019), Parkinson's disease (Lee et al., 2016), psychiatric disorders (Mai et al., 1993; Selemon and Begovic, 2007; Dorph-Petersen et al., 2009), as well as the MGB's involvement in tinnitus (Llinas et al., 2002; Rauschecker et al., 2010; Leaver et al., 2011; Ridder et al., 2015; Caspary and Llano, 2017; Berlot et al., 2020), and both structures' involvement in Leber's hereditary optic neuropathy (Jonak et al., 2020). In tinnitus patients, the maps have the potential to aid future neurosurgical planning for deep-brain stimulation (Smit et al., 2016; van Zwieten et al., 2021). The latter already benefits from the development of multimodal deep-brain stimulation atlases (Ewert et al., 2018) to which our metathalamic probability maps can contribute.

The high-resolution MGB BigBrain maps show the topography of the three subdivisions at nearly cellular resolution, and are interoperable with any reference space used in the neuroimaging community. This way, they can be used to bridge the microscale histology of the metathalamic BigBrain maps with macroscale functional measurements. Evidence from ultrahigh-field-fMRI studies for example shows a mirror-symmetric tonotopic gradient in the ventral MGB (Moerel et al., 2015), which is well reflected by the row-like cell clusters (Winer, 1984; Moerel et al., 2015) that were also detected in the BigBrain (**Figure 3B**). At the same time, the MGB and its ascending and descending connections seem to be involved in a tinnitus-related network (Rauschecker et al., 2010; Leaver et al., 2011; Caspary and Llano, 2017). Modulation of the ventral MGB is also behaviorally relevant for speech recognition (Mihai et al., 2019) explaining the MGB's involvement in developmental dyslexia (Díaz et al., 2012). The MGB BigBrain maps may facilitate studies of these larger scale involvements of thalamocortical circuits and local subcortical circuits.

Together with the already published LGB BigBrain maps (Brandstetter et al., 2021), the MGB maps provide a subcortical target space for neuroimaging data integration and comparative histological approaches at the level of specific subdivisions and layers of the metathalamus. Several studies have already used the 20-micron isotropic resolution of the BigBrain dataset for such integrative approaches (Paquola et al., 2020a; Royer et al., 2020) including subcortical structures of the auditory system (Sitek et al., 2019). The BigBrainWarp toolbox (Paquola et al., 2021, preprint) and the EBRAINS VoluBA toolbox for spatial anchoring in the BigBrain space[3] enable such an integration.

Such a relationship is not only relevant to support MR measurements with the cellular architecture, but also to develop better and more realistic human brain models. The incorporation of cytoarchitectonic parameters has recently led to more biologically valid models of the macaque visual system including cortical areas of different architectural types (Schmidt et al., 2018), as well as models of the human cerebellar granular layer (Florimbi et al., 2021). However, such models usually lack quantitative metathalamic input parameters, forcing them to be estimated indirectly based on other network parameters (Schmidt et al., 2018). Following this line of arguments, the metathalamic maps in the BigBrain can enrich current brain modeling approaches by directly extracting cytoarchitectonic features from the BigBrain (Paquola et al., 2020a; Dickscheid, 2021) at the cellular level (Dickscheid et al., 2019; Behuet et al., 2021). Recent advances in reconstructing the white matter fiber architecture from Nissl-stained glia cells (Schurr and Mezer, 2021) could allow to complement such features with sample specific connectivity data of layers and subdivisions of the metathalamus.

As the BigBrain dataset is continuously expanded by cortical and subcortical cytoarchitectonic parcellations, as well as intracortical surface models (DeKraker et al., 2020; Paquola et al., 2020a; Wagstyl et al., 2020), it provides an increasingly rich resource for such integrative approaches. The here provided high-resolution maps of the MGB contribute to this development.

DATA AVAILABILITY STATEMENT

The probability maps of the MGB and LGB (Kiwitz et al., 2021a,b) and the MGB BigBrain maps along with the respective reference delineations (Kiwitz et al., 2021c; Schiffer et al., 2021b) are available on EBRAINS: https://ebrains.eu/.

ETHICS STATEMENT

The studies involving human brain tissue from body donors were reviewed and approved by Ethics Committee of the Medical Faculty of the Heinrich Heine University Düsseldorf. The body donors provided written informed consent for the general use of their brain tissue for aims of research and education.

AUTHOR CONTRIBUTIONS

KK developed the concept for the manuscript, conducted the cytoarchitectonic brain mapping, validated the quality of the maps and wrote the manuscript. CS designed and implemented the deep-learning based brain mapping tool and created automatic mappings. AB validated the quality of the results of the MGB maps in the BigBrain and contributed LGB specific parts of the manuscript. SB conducted the comparative volumetric analysis of the ten postmortem brains and provided methodological advice. HM provided the calculations for image registration in the BigBrain dataset, calculated the probabilistic maps and integrated them into the Julich-Brain. PM and MO provided critical advice on 3D-visualizations and calculated smoothed volume meshes for the BigBrain maps. KA developed the concept of the study, coordinated the research, and provided neuroanatomical expertise. All authors contributed to the article and approved the submitted version.

SUPPLEMENTARY MATERIAL

The Supplementary Material for this article can be found online at: https://www.frontiersin.org/articles/10.3389/fnana.2022.837485/full#supplementary-material

Supplementary Video 1 | Zoom into the BigBrain model, left hemisphere, latero-caudal view (cutting plane corresponds to coronal section number 3290, rostral MGB). Subdivisions of the MGB are shown on the right, layers of the LGB are shown on the left.

REFERENCES

Amaral, L., Ganho-Ávila, A., Osório, A., Soares, M. J., He, D., Chen, Q., et al. (2016). Hemispheric asymmetries in subcortical visual and auditory relay structures in congenital deafness. *Eur. J. Neurosci.* 44, 2334–2339. doi: 10.1111/ejn.13340

Amunts, K., Armstrong, E., Malikovic, A., Hömke, L., Mohlberg, H., Schleicher, A., et al. (2007). Gender-specific left–right asymmetries in human visual cortex. *J. Neurosci.* 27, 1356–1364. doi: 10.1523/JNEUROSCI.4753-06.2007

Amunts, K., Lepage, C., Borgeat, L., Mohlberg, H., Dickscheid, T., Rousseau, M. -É, et al. (2013). BigBrain: an ultrahigh-resolution 3D human brain model. *Science* 340, 1472–1475. doi: 10.1126/science.1235381

Amunts, K., Mohlberg, H., Bludau, S., and Zilles, K. (2020). Julich-brain: a 3D probabilistic atlas of the human brain's cytoarchitecture. *Science* 369, 988–992. doi: 10.1126/science.abb4588

Amunts, K., Morosan, P., Hilbig, H., and Zilles, K. (2012). "Auditory system," in *The Human Nervous System*, eds J. K. Mai and G. Paxinos (Amsterdam: Elsevier Academic Press).

Andrews, T. J., Halpern, S. D., and Purves, D. (1997). Correlated size variations in human visual cortex, lateral geniculate nucleus, and optic tract. *J. Neurosci.* 17, 2859–2868. doi: 10.1523/JNEUROSCI.17-08-02859.1997

Behuet, S., Bludau, S., Kedo, O., Schiffer, C., Dickscheid, T., Brandstetter, A., et al. (2021). "A high-resolution model of the human entorhinal cortex in the 'BigBrain' – use case for machine learning and 3D analyses," in *Brain-Inspired Computing*, eds K. Amunts, L. Grandinetti, T. Lippert, and N. Petkov (Cham: Springer International Publishing), 3–21.

Berlot, E., Arts, R., Smit, J., George, E., Gulban, O. F., Moerel, M., et al. (2020). A 7 Tesla fMRI investigation of human tinnitus percept in cortical and subcortical auditory areas. *NeuroImage Clin.* 25, 102166. doi: 10.1016/j.nicl.2020.102166

Bernstein, A. S., Rapcsak, S. Z., Hornberger, M., and Saranathan, M. (2021). Structural changes in thalamic nuclei across prodromal and clinical Alzheimer's disease. *J. Alzheimers Dis. JAD* 82, 361–371. doi: 10.3233/JAD-201583

Bludau, S., Eickhoff, S. B., Mohlberg, H., Caspers, S., Laird, A. R., Fox, P. T., et al. (2014). Cytoarchitecture, probability maps and functions of the human frontal pole. *Neuroimage* 93(Pt 2), 260–275. doi: 10.1016/j.neuroimage.2013.05.052

Brandstetter, A., Bolakhrif, N., Schiffer, C., Dickscheid, T., Mohlberg, H., and Amunts, K. (2021). "Deep learning-supported cytoarchitectonic mapping of the human lateral geniculate body in the BigBrain," in *Brain-Inspired Computing*, eds K. Amunts, L. Grandinetti, T. Lippert, and N. Petkov (Cham: Springer International Publishing), 22–32.

Butler, B. E., and Lomber, S. G. (2013). Functional and structural changes throughout the auditory system following congenital and early-onset deafness: implications for hearing restoration. *Front. Syst. Neurosci.* 7:92. doi: 10.3389/fnsys.2013.00092

Butler, P. D., and Javitt, D. C. (2005). Early-stage visual processing deficits in schizophrenia. *Curr. Opin. Psychiatry* 18, 151–157. doi: 10.1097/00001504-200503000-00008

Caspary, D. M., and Llano, D. A. (2017). Auditory thalamic circuits and GABAA receptor function: Putative mechanisms in tinnitus pathology. *Hear. Res.* 349, 197–207. doi: 10.1016/j.heares.2016.08.009

Caspary, D. M., and Llano, D. A. (2019). "Aging processes in the subcortical auditory system," in *The Oxford Handbook of the Auditory Brainstem*, eds K. Kandler, D. M. Caspary, and D. A. Llano (Oxford: Oxford University Press), 638–680.

Cecchetti, L., Ricciardi, E., Handjaras, G., Kupers, R., Ptito, M., and Pietrini, P. (2016). Congenital blindness affects diencephalic but not mesencephalic structures in the human brain. *Brain Struct. Funct.* 221, 1465–1480. doi: 10.1007/s00429-014-0984-5

Clark, W. E. (1932). A morphological study of the lateral geniculate body. *Br. J. Ophthalmol.* 16, 264–284. doi: 10.1136/bjo.16.5.264

Clerici, W. J., and Coleman, J. R. (1990). Anatomy of the rat medial geniculate body: I. Cytoarchitecture, myeloarchitecture, and neocortical connectivity. *J. Comp. Neurol.* 297, 14–31. doi: 10.1002/cne.902970103

Dai, H., Mu, K. T., Qi, J. P., Wang, C. Y., Zhu, W. Z., Xia, L. M., et al. (2011). Assessment of lateral geniculate nucleus atrophy with 3T MR imaging and correlation with clinical stage of glaucoma. *Am. J. Neuroradiol.* 32, 1347–1353. doi: 10.3174/ajnr.A2486

DeKraker, J., Lau, J. C., Ferko, K. M., Khan, A. R., and Köhler, S. (2020). Hippocampal subfields revealed through unfolding and unsupervised clustering of laminar and morphological features in 3D BigBrain. *Neuroimage* 206:116328. doi: 10.1016/j.neuroimage.2019.116328

Díaz, B., Hintz, F., Kiebel, S. J., and Von Kriegstein, K. (2012). Dysfunction of the auditory thalamus in developmental dyslexia. *Proc. Natl. Acad. Sci. U.S.A.* 109, 13841–13846. doi: 10.1073/pnas.1119828109

Dickscheid, T. (2021). *siibra – Python Interface for Interacting With Brain Atlases*. Available online at: https://github.com/FZJ-INM1-BDA/siibra-python (accessed December 16, 2021).

Dickscheid, T., Haas, S., Bludau, S., Glock, P., Huysegoms, M., and Amunts, K. (2019). Towards 3D reconstruction of neuronal cell distributions from histological human brain sections. *Adv. Paral. Comput.* 34, 223–239. doi: 10.3233/APC190016

Ding, S.-L., Royall, J. J., Sunkin, S. M., Ng, L., Facer, B. A. C., Lesnar, P., et al. (2016). Comprehensive cellular-resolution atlas of the adult human brain. *J. Comp. Neurol.* 524, 3127–3481. doi: 10.1002/cne.24080

Dorph-Petersen, K.-A., Caric, D., Saghafi, R., Zhang, W., Sampson, A. R., and Lewis, D. A. (2009). Volume and neuron number of the lateral geniculate nucleus in schizophrenia and mood disorders. *Acta Neuropathol.* 117, 369–384. doi: 10.1007/s00401-008-0410-2

Eidelberg, D., and Galaburda, A. M. (1982). Symmetry and asymmetry in the human posterior thalamus. I. Cytoarchitectonic analysis in normal persons. *Arch. Neurol.* 39, 325–332. doi: 10.1001/archneur.1982.00510180003001

Evans, A. C., Janke, A. L., Collins, D. L., and Baillet, S. (2012). Brain templates and atlases. *Neuroimage* 62, 911–922. doi: 10.1016/j.neuroimage.2012.01.024

Ewert, S., Plettig, P., Li, N., Chakravarty, M. M., Collins, D. L., Herrington, T. M., et al. (2018). Toward defining deep brain stimulation targets in MNI space: a subcortical atlas based on multimodal MRI, histology and structural connectivity. *Neuroimage* 170, 271–282. doi: 10.1016/j.neuroimage.2017.05.015

Florimbi, G., Torti, E., Masoli, S., D'Angelo, E., and Leporati, F. (2021). Granular layer simulator: Design and multi-GPU simulation of the cerebellar granular layer. *Front. Comput. Neurosci.* 15:630795. doi: 10.3389/fncom.2021.630795

García-Gomar, M. G., Strong, C., Toschi, N., Singh, K., Rosen, B. R., Wald, L. L., et al. (2019). *In vivo* probabilistic structural atlas of the inferior and superior colliculi, medial and lateral geniculate nuclei and superior olivary complex in humans based on 7 Tesla MRI. *Front. Neurosci.* 13:764. doi: 10.3389/fnins.2019.00764

Glendenning, K. K., and Masterton, R. B. (1998). Comparative morphometry of mammalian central auditory systems: variation in nuclei and form of the ascending system. *BBE* 51, 59–89. doi: 10.1159/000006530

Harrison, J. M., and Howe, M. E. (1974). "Anatomy of the afferent auditory nervous system of mammals," in *Auditory System*, eds H. W. Ades, A. Axelsson, I. L. Baird, G. v Békésy, R. L. Boord, C. B. G. Campbell, et al. (Berlin: Springer Berlin Heidelberg), 283–336.

Hassler, R. (1959). "Anatomy of the thalamus," in *Introduction to Stereotaxic Operations With an Atlas of the Human Brain*, eds G. Schaltenbrand and P. Bailey (New York, NY: Georg Thieme Verlag).

Hickman, S. J., Raoof, N., McLean, R. J., and Gottlob, I. (2014). Vision and multiple sclerosis. *Multip. Scleros. Relat. Disord.* 3, 3–16. doi: 10.1016/j.msard.2013.04.004

Huber, L., Tse, D. H. Y., Wiggins, C. J., Uludağ, K., Kashyap, S., Jangraw, D. C., et al. (2018). Ultra-high resolution blood volume fMRI and BOLD fMRI in humans at 9.4 T: capabilities and challenges. *Neuroimage* 178, 769–779. doi: 10.1016/j.neuroimage.2018.06.025

Iglesias, J. E., Insausti, R., Lerma-Usabiaga, G., Bocchetta, M., van Leemput, K., Greve, D. N., et al. (2018). A probabilistic atlas of the human thalamic nuclei combining ex vivo MRI and histology. *Neuroimage* 183, 314–326. doi: 10.1016/j.neuroimage.2018.08.012

Jia, K., Zamboni, E., Rua, C., Goncalves, N. R., Kemper, V., Ng, A. K. T., et al. (2021). A protocol for ultra-high field laminar fMRI in the human brain. *STAR Protoc.* 2:100415. doi: 10.1016/j.xpro.2021.100415

Jonak, K., Krukow, P., Jonak, K. E., Radzikowska, E., Baj, J., Niedziałek, A., et al. (2020). Decreased volume of lateral and medial geniculate nuclei in patients with LHON disease-7 Tesla MRI study. *J. Clin. Med.* 9:2914. doi: 10.3390/jcm9092914

Kitajima, M., Hirai, T., Yoneda, T., Iryo, Y., Azuma, M., Tateishi, M., et al. (2015). Visualization of the medial and lateral geniculate nucleus on phase difference enhanced imaging. *Am. J. Neuroradiol.* 36, 1669–1674. doi: 10.3174/ajnr.A4356

Kiwitz, K., Mohlberg, H., Brandstetter, A., Bludau, S., and Amunts, K. (2021a). *Probabilistic Cytoarchitectonic Map of the Human Corpus geniculatum laterale (CGL, LGB, Metathalamus) [Data set]*. EBRAINS. doi: 10.25493/1H7R-M3R

Kiwitz, K., Mohlberg, H., Brandstetter, A., Bludau, S., and Amunts, K. (2021b). *Probabilistic Cytoarchitectonic Map of the Human Corpus geniculatum mediale (CGM, MGB, Metathalamus) [Data set]*. EBRAINS. doi: 10.25493/75TH-FE9

Kiwitz, K., Schiffer, C., Brandstetter, A., Mohlberg, H., Amunts, K., and Dickscheid, T. (2021c). *Reference Delineations of the Human Corpus Geniculatum Mediale (CGM, MGB, MGBv, MGBd, MGBm, Metathalamus) in Individual Sections of the BigBrain*. EBRAINS. doi: 10.25493/3SM6-HGM

Kiwitz, K., Schiffer, C., Spitzer, H., Dickscheid, T., and Amunts, K. (2020). Deep learning networks reflect cytoarchitectonic features used in brain mapping. *Sci. Rep.* 10:22039. doi: 10.1038/s41598-020-78638-y

Korsholm, K., Madsen, K. H., Frederiksen, J. L., Skimminge, A., and Lund, T. E. (2007). Recovery from optic neuritis: an ROI-based analysis of LGN and visual cortical areas. *Brain* 130, 1244–1253. doi: 10.1093/brain/awm045

Krause, D., and Thörnig, P. (2018). JURECA: modular supercomputer at jülich supercomputing centre. *JLSRF* 4:132. doi: 10.17815/jlsrf-4-121-1

Krauth, A., Blanc, R., Poveda, A., Jeanmonod, D., Morel, A., and Székely, G. (2010). A mean three-dimensional atlas of the human thalamus: generation from multiple histological data. *Neuroimage* 49, 2053–2062. doi: 10.1016/j. neuroimage.2009.10.042

Kuhlenbeck, H. (1954). The human diencephalon; a summary of development, structure, function, and pathology. *Confin. Neurol* 14, 1–230.

Leaver, A. M., Renier, L., Chevillet, M. A., Morgan, S., Kim, H. J., and Rauschecker, J. P. (2011). Dysregulation of limbic and auditory networks in tinnitus. *Neuron* 69, 33–43. doi: 10.1016/j.neuron.2010.12.002

Lee, J.-Y., Yoon, E. J., Lee, W. W., Kim, Y. K., Lee, J.-Y., and Jeon, B. (2016). Lateral geniculate atrophy in Parkinson's with visual hallucination: a trans-synaptic degeneration? *Mov. Disord.* 31, 547–554. doi: 10.1002/mds.26533

Lewiner, T., Lopes, H., Vieira, A. W., and Tavares, G. (2003). Efficient implementation of marching cubes' cases with topological guarantees. *J. Graph. Tools* 8, 1–15. doi: 10.1080/10867651.2003.10487582

Li, M., He, H. G., Shi, W., Li, J., Lv, B., Wang, C. H., et al. (2012). Quantification of the human lateral geniculate nucleus *in vivo* using MR imaging based on morphometry: volume loss with age. *Am. J. Neuroradiol.* 33, 915–921. doi: 10.3174/ajnr.A2884

Lin, F. R., Ferrucci, L., An, Y., Goh, J. O., Doshi, J., Metter, E. J., et al. (2014). Association of hearing impairment with brain volume changes in older adults. *Neuroimage* 90, 84–92. doi: 10.1016/j.neuroimage.2013.12.059

Llano, D. A., and Sherman, S. M. (2008). Evidence for nonreciprocal organization of the mouse auditory thalamocortical-corticothalamic projection systems. *J. Compar. Neurol.* 507, 1209–1227. doi: 10.1002/cne.21602

Llinas, R. R., Leznik, E., and Urbano, F. J. (2002). Temporal binding *via* cortical coincidence detection of specific and nonspecific thalamocortical inputs: a voltage-dependent dye-imaging study in mouse brain slices. *Proc. Natl. Acad. Sci. U.S.A.* 99, 449–454. doi: 10.1073/pnas.012604899

Mai, J. K., Berger, K., and Sofroniew, M. V. (1993). Morphometric evaluation of neurophysin-immunoreactivity in the human brain: pronounced inter-individual variability and evidence for altered staining patterns in schizophrenia. *J. Hirnforsch.* 34, 133–154.

Mai, J. K., Majtanik, M., and Paxinos, G. (2016). *Atlas of the Human Brain*. Amsterdam: Elsevier AP.

Margulies, D. S., Ghosh, S. S., Goulas, A., Falkiewicz, M., Huntenburg, J. M., Langs, G., et al. (2016). Situating the default-mode network along a principal gradient of macroscale cortical organization. *Proc. Natl. Acad. Sci. U.S.A.* 113, 12574–12579. doi: 10.1073/pnas.1608282113

Martino, F., de Moerel, M., Ugurbil, K., Goebel, R., Yacoub, E., and Formisano, E. (2015). Frequency preference and attention effects across cortical depths in the human primary auditory cortex. *Proc. Natl. Acad. Sci. U.S.A.* 112, 16036–16041. doi: 10.1073/pnas.1507552112

Merker, B. (1983). Silver staining of cell bodies by means of physical development. *J. Neurosci. Methods* 9, 235–241. doi: 10.1016/0165-0270(83)90086-9

Mihai, P. G., Moerel, M., Martino, F., de Trampel, R., Kiebel, S., and von Kriegstein, K. (2019). Modulation of tonotopic ventral medial geniculate body is behaviorally relevant for speech recognition. *eLife Sci.* 8:44837. doi: 10.7554/eLife.44837

Moerel, M., Martino, F., de Uðurbil, K., Yacoub, E., and Formisano, E. (2015). Processing of frequency and location in human subcortical auditory structures. *Sci. Rep.* 5:17048. doi: 10.1038/srep17048

Morel, A. (2007). *Stereotactic Atlas of the Human Thalamus and Basal Ganglia*. New York, NY: Informa Healthcare.

Morest, D. K. (1964). The neuronal architecture of the medial geniculate body of the cat. *J. Anat.* 98, 611–630.

Najdenovska, E., Alemán-Gómez, Y., Battistella, G., Descoteaux, M., Hagmann, P., Jacquemont, S., et al. (2018). *In-vivo* probabilistic atlas of human thalamic nuclei based on diffusion- weighted magnetic resonance imaging. *Sci. Data* 5:180270. doi: 10.1038/sdata.2018.270

Nasr, S., Polimeni, J. R., and Tootell, R. B. H. (2016). Interdigitated color- and disparity-selective columns within human visual cortical areas V2 and V3. *J. Neurosci.* 36, 1841–1857. doi: 10.1523/JNEUROSCI.3518-15.2016

Omidyeganeh, M., Lepage, C., Wagstyl, K., Spitzer, H., Dickscheid, T., Amunts, K., et al. (2020). "Non-linear registration of 1µm histology sections into 3D 20µm BigBrain space," in *2020 Organization for Human Brain Mapping Annual Meeting: A Virtual Experience for Engaging Minds & Empowering Brain Science*, ed. Organization for Human Brain Mapping (Minneapolis, MN: Organization for Human Brain Mapping).

Papadopoulou, A., Gaetano, L., Pfister, A., Altermatt, A., Tsagkas, C., Morency, F., et al. (2019). Damage of the lateral geniculate nucleus in MS: assessing the missing node of the visual pathway. *Neurology* 92, e2240–e2249. doi: 10.1212/WNL.0000000000007450

Paquola, C., Seidlitz, J., Benkarim, O., Royer, J., Klimes, P., Bethlehem, R. A. I., et al. (2020b). A multi-scale cortical wiring space links cellular architecture and functional dynamics in the human brain. *PLoS Biol.* 18:e3000979. doi: 10.1371/journal.pbio.3000979

Paquola, C., Benkarim, O., DeKraker, J., Larivière, S., Frässle, S., Royer, J., et al. (2020a). Convergence of cortical types and functional motifs in the human mesiotemporal lobe. *eLife Sci.* 9:60673. doi: 10.7554/eLife.60673

Paquola, C., Royer, J., Lewis, L. B., Lepage, C., Glatard, T., Wagstyl, K., et al. (2021). BigBrainWarp: toolbox for integration of BigBrain 3D histology with multimodal neuroimaging. *bioRxiv* [Preprint]. Available online at: https://www.biorxiv.org/content/10.1101/2021.05.04.442563v1 (accessed December 16, 2021).

Paquola, C., Vos De Wael, R., Wagstyl, K., Bethlehem, R. A. I., Hong, S.-J., Seidlitz, J., et al. (2019). Microstructural and functional gradients are increasingly dissociated in transmodal cortices. *PLoS Biol.* 17:e3000284. doi: 10.1371/journal.pbio.3000284

Pasu, S., Ridha, B. H., Wagh, V., Jindahra, P., Siddiqui, A., Plant, G., et al. (2015). Homonymous sectoranopia: asymptomatic presentation of a lateral geniculate nucleus lesion. *Neuroophthalmology* 39, 289–294. doi: 10.3109/01658107.2015.1079221

Peruzzi, D., Bartlett, E., Smith, P. H., and Oliver, D. L. (1997). A monosynaptic GABAergic input from the inferior colliculus to the medial geniculate body in rat. *J. Neurosci.* 17, 3766–3777. doi: 10.1523/JNEUROSCI.17-10-03766.1997

Qian, Z. J., Chang, P. D., Moonis, G., and Lalwani, A. K. (2017). A novel method of quantifying brain atrophy associated with age-related hearing loss. *NeuroImage Clin.* 16, 205–209. doi: 10.1016/j.nicl.2017.07.021

Rademacher, J., Bürgel, U., and Zilles, K. (2002). Stereotaxic localization, intersubject variability, and interhemispheric differences of the human auditory thalamocortical system. *Neuroimage* 17, 142–160. doi: 10.1006/nimg.2002.1178

Rauschecker, J. P., Leaver, A. M., and Mühlau, M. (2010). Tuning out the noise: limbic-auditory interactions in tinnitus. *Neuron* 66, 819–826. doi: 10.1016/j. neuron.2010.04.032

Ridder, D., de Vanneste, S., Langguth, B., and Llinas, R. (2015). Thalamocortical dysrhythmia: a theoretical update in tinnitus. *Front. Neurol.* 6:124. doi: 10.3389/fneur.2015.00124

Rijk, M. M., de van den Hurk, J., Rahnama'i, M. S., and van Koeveringe, G. A. (2021). Parcellation of human periaqueductal gray at 7-T fMRI in full and empty bladder state: the foundation to study dynamic connectivity changes related to lower urinary tract functioning. *Neurourol. Urodynam.* 40, 616–623. doi: 10.1002/nau.24602

Royer, J., Paquola, C., Larivière, S., Vos De Wael, R., Tavakol, S., Lowe, A. J., et al. (2020). Myeloarchitecture gradients in the human insula: Histological underpinnings and association to intrinsic functional connectivity. *Neuroimage* 216:116859. doi: 10.1016/j.neuroimage.2020.116859

Saint Marie, R. L., Stanforth, D., and Jubelier, E. (1997). Substrate for rapid feedforward inhibition of the auditory forebrain. *Brain Res.* 765, 173–176. doi: 10.1016/S0006-8993(97)00654-9

Schiffer, C., Spitzer, H., Kiwitz, K., Unger, N., Wagstyl, K., Evans, A. C., et al. (2021c). Convolutional neural networks for cytoarchitectonic brain mapping at large scale. *Neuroimage* 240:118327. doi: 10.1016/j.neuroimage.2021.118327

Schiffer, C., Brandstetter, A., Bolakhrif, N., Mohlberg, H., Amunts, K., and Dickscheid, T. (2021a). *Ultrahigh Resolution 3D Cytoarchitectonic Map of the LGB (Lam 1-6, CGL, Metathalamus) Created by a Deep-Learning Assisted Workflow*. EBRAINS. doi: 10.25493/33Z0-BX

Schiffer, C., Kiwitz, K., Brandstetter, A., Mohlberg, H., Amunts, K., and Dickscheid, T. (2021b). *Ultrahigh Resolution 3D Cytoarchitectonic map of the Human Corpus*

Geniculatum Mediale (CGM, MGB, MGBv, MGBd, MGBm, Metathalamus). EBRAINS. doi: 10.25493/PNY0-NCW

Schmidt, M., Bakker, R., Shen, K., Bezgin, G., Diesmann, M., and van Albada, S. J. (2018). A multi-scale layer-resolved spiking network model of resting-state dynamics in macaque visual cortical areas. *PLoS Comput. Biol.* 14:e1006359. doi: 10.1371/journal.pcbi.1006359

Schurr, R., and Mezer, A. A. (2021). The glial framework reveals white matter fiber architecture in human and primate brains. *Science* 374, 762–767. doi: 10.1126/science.abj7960

Selemon, L. D., and Begovic, A. (2007). Stereologic analysis of the lateral geniculate nucleus of the thalamus in normal and schizophrenic subjects. *Psychiatry Res.* 151, 1–10. doi: 10.1016/j.psychres.2006.11.003

Sepulcre, J., Goñi, J., Masdeu, J. C., Bejarano, B., Vélez de Mendizábal, N., Toledo, J. B., et al. (2009). Contribution of white matter lesions to gray matter atrophy in multiple sclerosis: evidence from voxel-based analysis of T1 lesions in the visual pathway. *Arch. Neurol.* 66, 173–179. doi: 10.1001/archneurol.2008.562

Sitek, K. R., Gulban, O. F., Calabrese, E., Johnson, G. A., Lage-Castellanos, A., Moerel, M., et al. (2019). Mapping the human subcortical auditory system using histology, postmortem MRI and in vivo MRI at 7T. *eLife* 8:e48932. doi: 10.7554/eLife.48932

Smit, J. V., Janssen, M. L. F., van Zwieten, G., Jahanshahi, A., Temel, Y., and Stokroos, R. J. (2016). Deep brain stimulation of the inferior colliculus in the rodent suppresses tinnitus. *Brain Res.* 1650, 118–124. doi: 10.1016/j.brainres.2016.08.046

Stanton, S. G., and Harrison, R. V. (2000). Projections from the medial geniculate body to primary auditory cortex in neonatally deafened cats. *J. Compar. Neurol.* 426, 117–129. doi: 10.1002/1096-9861(20001009)426:1<117:AID-CNE8>3.0.CO;2-S

Stein, J. D., Khawaja, A. P., and Weizer, J. S. (2021). Glaucoma in adults-screening, diagnosis, and management: a review. *JAMA* 325, 164–174. doi: 10.1001/jama.2020.21899

Strick, P. L., and Sterling, P. (1974). Synaptic termination of afferents from the ventrolateral nucleus of the thalamus in the cat motor cortex. A light and electron microscopy study. *J. Comp. Neurol.* 153, 77–106. doi: 10.1002/cne.901530107

Usrey, W. M., and Alitto, H. J. (2015). Visual functions of the thalamus. *Annu. Rev. Vis. Sci.* 1, 351–371. doi: 10.1146/annurev-vision-082114-035920

van Zwieten, G., Roberts, M. J., Schaper, F. L. V. W., Smit, J. V., Temel, Y., and Janssen, M. L. F. (2021). Noise-induced neurophysiological alterations in the rat medial geniculate body and thalamocortical desynchronization by deep brain stimulation. *J. Neurophysiol.* 125, 661–671. doi: 10.1152/jn.00752.2019

Wagstyl, K., Larocque, S., Cucurull, G., Lepage, C., Cohen, J. P., Bludau, S., et al. (2020). BigBrain 3D atlas of cortical layers: cortical and laminar thickness gradients diverge in sensory and motor cortices. *PLoS Biol.* 18:e3000678. doi: 10.1371/journal.pbio.3000678

Wang, J., Miao, W., Li, J., Li, M., Zhen, Z., Sabel, B., et al. (2015). Automatic segmentation of the lateral geniculate nucleus: application to control and glaucoma patients. *J. Neurosci. Methods* 255, 104–114. doi: 10.1016/j.jneumeth.2015.08.006

Wei, Y., Scholtens, L. H., Turk, E., and van den Heuvel, M. P. (2019). Multiscale examination of cytoarchitectonic similarity and human brain connectivity. *Netw. Neurosci.* 3, 124–137. doi: 10.1162/netn_a_00057

Winer, J. A. (1984). The human medial geniculate body. *Hear. Res.* 15, 225–247. doi: 10.1016/0378-5955(84)90031-5

Winer, J. A. (1992). "The functional architecture of the medial geniculate body and the primary auditory cortex," in *The Mammalian Auditory Pathway: Neuroanatomy*, eds R. R. Fay, A. N. Popper, and D. B. Webster (New York, NY: Springer New York), 222–409.

Wong, C., Chabot, N., Kok, M. A., and Lomber, S. G. (2014). Modified areal cartography in auditory cortex following early- and late-onset deafness. *Cereb. Cortex* 24, 1778–1792. doi: 10.1093/cercor/bht026

Zvorykin, V. P. (1980). Novoe v voprose ob individual'nykh kolichestvennykh osobennostiakh lateral'nogo kolenchatogo tela cheloveka. *Arkh. Anat. Gistol. Embriol.* 78, 24–27.